11th International Symposium on Turbulence and Shear Flow Phenomena (TSFP11)
Southampton, UK, July 30 to August 2, 2019

PREDICTION OF PARTICULATE FOULING ON STRUCTURED SURFACES USING MULTIPHASE EULERIAN-LAGRANGIAN LES

Robert Kasper, Johann Turnow, Nikolai Kornev
Chair of Modeling and Simulation
Department of Mechanical Engineering and Marine Technology
University of Rostock
Albert-Einstein-Str. 2, 18059 Rostock - Germany
robert.kasper@uni-rostock.de

ABSTRACT

This paper presents the application of multiphase Eulerian-Lagrangian Large-Eddy Simulations (LES) for the prediction of particulate fouling on structured surfaces. An efficient Lagrangian-Particle-Tracking algorithm is used to predict the trajectories of supended the foulant particles (dispersed phase), suitable for dilute and dense dispersed two-phase flows by taking the fluid-particle (two-way coupling) as well as inter-particle interactions (four-way coupling) into account. The turbulent carrier flow (continuous phase) is calculated by eddy-resolving LES. Calculations have been performed for fully developed turbulent channel flows at moderate Reynolds numbers in combination with different sharp-edged, spherical dimple packages considering dimple depth/diameter ratios of $t/D = 0.26 - 0.36$.

INTRODUCTION

Structured surfaces such as ribs, pin fins, dimples and protrusions are extensively used heat transfer enhancement techniques, especially in compact heat exchangers, which reduce the thermal resistance of the sublayer adjacent to solid walls. This is achieved by generating secondary flows, which interfere the boundary layer growth, as well as flow recirculation and shear-layer reattachment, promoting mixing and an increase of the turbulence intensity. Various types of structured heat transfer surfaces have been thoroughly investigated with the objective to promote the heat transfer with a minimum hydraulic pressure loss. The application of dimpled surfaces is an efficient way to increase the thermo-hydraulic performance, defined as ratio between heat exchange and flow resistance, revealing a significant heat transfer augmentation at low pressure drop penalty. A significant issue of structured surfaces is the enhancement of undesired deposition of crystals, microorganism or particles from the fluid. This phenomenon is referred to as particluate Fouling. Fouling on heat exchanging surfaces reduces the efficiency of heat exchangers and increases flow resistance leading to a decrease of the thermo-hydraulic efficiency. That potentially results in higher technical and economical effort like higher costs in energy or maintenance (Bohnet (1987)). Besides crystallization fouling particulate fouling is one of the main reasons for efficiency problems. The suspended particles in the heat exchanging fluid are for instance corrosion products, sand or mud (Müller-Steinhagen (2010)). The objective of this investigation is to clarify the role of turbulent flow structures generated by dimpled surfaces with respect to mass transport and particulate fouling using large-scale resolving Eulerian-Lagrangian LES and high-precision fouling measurements.

COMPUTATIONAL METHODOLOGY

The underlying numerical procedure for the simulation of particulate fouling is based on the Eulerian-Lagrangian approach. Large-scale resolving LES are used to predict the continuous phase with respect to the local fouling layer in an Eulerian frame of reference. The dispersed phase is tracked within the computational domain in a Lagrangian frame, also referred to as Lagrangian-Particle-Tracking (LPT). The formation of fouling deposits is realized by a particle deposition model based on a local energy balance around the particle-wall/particle-fouling collision. Additionally, a sub-model based on the local wall shear stress is implemented to take the removal of the fouling deposits and re-entrainment of deposited particles into account.

The carrier fluid is assumed incompressible, Newtonian and the impact of the fluid temperature T on the thermophysical fluid and particle properties is neglected. Thus, the fluid phase is fully described by the following LES equations, which can be derived by applying an implicit-box filter (filter width $\overline{\Delta}$ is given by the underlying numerical grid) on the governing Navier-Stokes equations as well as on the simplified energy equation:

$$\nabla \cdot \overline{\mathbf{u}} = 0, \tag{1}$$

$$\frac{\partial \overline{\mathbf{u}}}{\partial t} + \nabla \cdot (\overline{\mathbf{u}}\,\overline{\mathbf{u}}) = -\frac{1}{\rho}\nabla p + \nu \nabla^2 \overline{\mathbf{u}} - \nabla \cdot \tau_{SGS} - \overline{\mathbf{S}}_P(\alpha) + \overline{\mathbf{S}}_M, \tag{2}$$

$$\frac{\partial \overline{T}}{\partial t} + \nabla \cdot \left(\overline{\mathbf{u}}\overline{T}\right) = \nabla \cdot \left(a(\alpha)\nabla \overline{T}\right) - \nabla \cdot \mathbf{q}_{SGS}, \tag{3}$$

where $\overline{\mathbf{u}}$ is the filtered fluid velocity, $\overline{T}$ is the filtered fluid temperature, $a(\alpha)$ is the thermal diffusivity as function of the so-called fouling phase fraction:

$$\alpha = \frac{\sum_i V_{p,i}}{V_c}, \tag{4}$$

which is the ratio of the summarized particle volume $\sum_i V_{p,i}$ inside the considered computational grid cell to the total volume of the mesh cell V_c, respectively, and varies from 0 (no fouling within the cell) to 1 (cell is fully filled with fouling). Based on the introduced fouling phase fraction α, each thermophysical property ϕ (e.g. density, thermal conductivity) is individually determined, for each grid cell, using the following interpolation:

$$\phi = \alpha\phi_{fouling} + (1-\alpha)\phi_{fluid}. \tag{5}$$

On the right-hand side of Eq. (2), the porosity source term $\overline{\mathbf{S}}_P = \alpha\frac{\overline{\mu}}{K}\overline{\mathbf{u}}$, which accounts for the additional hydraulic losses (contraction of the channel cross section) due to the settled fouling layer, is introduced.

The subgrid-scale stress tensor $\tau_{SGS} = \overline{\mathbf{u}\mathbf{u}} - \overline{\mathbf{u}}\,\overline{\mathbf{u}}$ in Eq. (2) is modeled using a dynamic one equation eddy-viscosity model proposed by Yoshizawa and Horiuti (Yoshizawa (1982); Yoshizawa & Horiuti (1985)) and Kim and Menon (Kim & Menon (1995)). This model uses a modeled balance equation, based on the assumption of SGS isotropy, to determine the distribution of the SGS kinetic energy $k_{SGS} = \mathrm{tr}\left(\tau_{SGS}\right)/2$:

$$\frac{\partial k_{SGS}}{\partial t} + \nabla\cdot\left(k_{SGS}\overline{\mathbf{u}}\right) = \nabla\cdot\left[(\nu+\nu_{SGS})\nabla k_{SGS}\right] - \tau_{SGS} : \overline{\mathbf{S}} - \varepsilon, \tag{6}$$

in which the dynamic procedure of Germano et al. (Germano *et al.* (1991)) is applied to evaluate all required coefficients dynamically in space and time, to avoid the application of damping functions (e.g. Van Driest damping) in the vicinity of solid walls. The dissipation ε, the SGS eddy-viscosity ν_{SGS} and the resulting modeled SGS stress tensor τ_{SGS} can be determined from the following relations:

$$\varepsilon = C_\varepsilon k_{SGS}^{3/2}\overline{\Delta}, \tag{7}$$

$$\nu_{SGS} = C_k k_{SGS}^{1/2}\overline{\Delta}, \tag{8}$$

$$\tau_{SGS} = -2\nu_{SGS}\overline{\mathbf{S}} + 2/3 k_{SGS}\mathbf{I}. \tag{9}$$

Additionally, the subgrid-scale heat flux $\mathbf{q}_{SGS} = \overline{\mathbf{u}T} - \overline{\mathbf{u}}\overline{T}$ in Eq. (3) is considered using the gradient-diffusion hypothesis, which is frequently used in numerical simulations of turbulent flows involving transport equations (da Silva & Pereira (2007); Combest *et al.* (2011)).

The Lagrangian particle tracking is applied to calculate the particle velocity and location during the simulations. Within this framework, the motion equations for isothermal particles in their most fundamental form have to be solved:

$$\frac{\mathrm{d}\mathbf{x}_p}{\mathrm{d}t} = \mathbf{u}_p, \tag{10}$$

$$m_p\frac{\mathrm{d}\mathbf{u}_p}{\mathrm{d}t} = \sum\mathbf{F}, \tag{11}$$

where m_p is the particle mass and $\mathbf{F}$ includes all external aerodynamic or hydrodynamic forces acting on the particle (e.g. drag, gravity, lift force) and forces resulting from particle-particle and particle-wall collisions. The foulant particles are assumed to be spherical and rigid. The drag force, being the dominating force in most fluid-particle systems Sommerfeld (2010), is calculated in terms of a drag coefficient C_D, allowing the determination of the drag force for different flow regimes (Stokes regime, transition and fully turbulent region). The implemented drag model is based on the particle Reynolds number, which is defined as

$$Re_p = \frac{\rho_f D_p\left|\mathbf{u}_f - \mathbf{u}_p\right|}{\mu_f}, \tag{12}$$

with the density ρ_f and the dynamic viscosity μ_f of the fluid or continuous phase, the particle diameter D_p and the magnitude of the relative slip velocity $\left|\mathbf{u}_f - \mathbf{u}_p\right|$. According to Eq. (12), the drag coefficient is determined using the drag correlation proposed by Putnam (Putnam (1961)):

$$C_D = \begin{cases} \frac{24}{Re_p}\left(1+\frac{1}{6}Re_p^{2/3}\right) & \text{if} \quad Re_p \leq 1,000 \\ 0.424 & \text{if} \quad Re_p > 1,000, \end{cases} \tag{13}$$

which is suitable to higher Reynolds numbers and ensures the correct limiting behavior within the fully turbulent regime. The general force representation is used to evaluate the drag force for spherical particles:

$$\mathbf{F_D} = C_D\frac{\pi D_p^2}{8}\rho_f\left(\mathbf{u}_f - \mathbf{u}_p\right)\left|\mathbf{u}_f - \mathbf{u}_p\right|. \tag{14}$$

Further particle force models are implemented to consider additional particle forces as gravity and buoyancy, pressure gradient force, added mass force, lift forces (Saffman) and thermophoretic force. Four-way coupling is provided through a time-dependent volume-averaged source term $\overline{\mathbf{S}}_m$, based on the PSI-CELL (Particle-Source-In Cell) approach (Crowe *et al.* (1977)), in Eq. (2), and a modified Cundall-Strack model proposed by Tsuji et al. (Tsuji *et al.* (1992)) to resolve the particle-particle interactions.

The formation of fouling deposits is modeled using a deposition sub-model, which balances the local forces (e.g. London-Van der Waals forces and electrostatic double-layer interaction forces) around the particle-wall/particle-fouling collision. Based on this approach the particle-stick condition is fulfilled, if the actual particle velocity falls below a certain critical stick velocity. Afterwards, the sticking particle is converted into a second, porous continuous phase (fouling phase), according to Eq. (4), and will be removed from the LPT, which decreases the computational effort and enhances the applicability of the proposed approach. A sub-model, based on a model proposed by Kern and Seaton (Kern & Seaton (1959)) and Taborek et al. (Taborek *et al.* (1984)), is implemented to consider the removal of fouling deposits and the re-entrainment of deposited fouling particles.

Further information according to the particle deposition and removal sub-models as well as for the conversion algorithm (including validation and verification of the numerical methods) can be found in (Kasper *et al.* (2017, 2018)).

RESULTS

The computational domain for the particle-laden turbulent channel flow over dimples in a staggered arrangement (dimple package) is given in Figure 1, with a size of $9.936H \times H \times 9.936H$ in $x-$, $y-$ and $z-$direction and a channel height of $H = 0.015\,\mathrm{m}$. The sharp-edged spherical dimples have a uniform dimple diameter of $D =$

0.046 m and the distance between neighboring dimples is $S = 0.81D$. Two different dimple depth-to-diameter ratios, namely $t/D = 0.26$ and 0.35 were considered in this study.

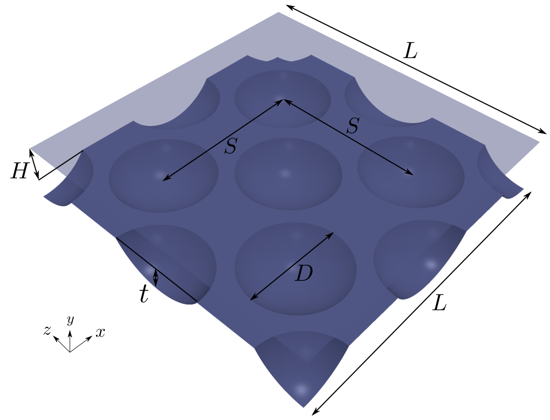

Figure 1. Sketch of the computational domain for the turbulent particle-laden channel flow over sharp-edged spherical dimples in a staggered arrangement.

Periodic boundary conditions are imposed in streamwise (x) and spanwise direction (z), whereas no-slip conditions are applied at the lower and upper channel walls. The structured, bottom wall is heated through a constant, non-dimensional temperature $T^+ = (T - T_\infty)/(T_w - T_\infty) = 1$ and the smooth, opposite channel wall is cooled with $T^+ = 0$. The molecular Prandtl number Pr is set to 0.71, whereas the turbulent Prandtl number Pr_t is 0.9. The corresponding Reynolds number is $Re_D = u_b D/\nu = 42{,}000$ based on the averaged bulk velocity $u_b = 0.91\,\mathrm{m/s}$ and the dimple print diameter D. Based on the LES results, shown in Figure 2, from a series of preliminary simulations for a smooth, narrow channel flow with a corresponding shear Reynolds number of $Re_\tau = 395$ and equal dimensions as for the channel flow with the dimple arrangement at the bottom wall, the computational domain is spatially discretized by a block-structured curvilinear grid consisting of $8{,}529{,}920$ hexahedral cells. A moderate, linear grid stretching in wall normal direction (y) is used to place the first grid node inside of the laminar sublayer at $y^+ \approx 1$. Spherical, mono-dispersed glass beads with a particle diameter of $D_p = 20\,\mu$m, typical for fouling related problems, and a density ratio of $\rho_p/\rho_f \approx 2.5$ are randomly injected at the domain inlet. Based on earlier experimental fouling investigations on heat exchangers (Blöchl & Müller-Steinhagen (1990)), a particle mass loading of $\eta = \dot{m}_p/\dot{m}_f = 0.1\%$ and 0.2% is chosen to ensure an asymptotic fouling layer growth and steady-state fouling conditions within a few minutes of physical real time. Particle motions are computed considering drag, lift, gravity and buoyancy, added mass as well as thermophoresis and pressure gradient force. Due to the low volume fraction of the dispersed phase, the neglect of inter-particle collisions is assumed and only two-way phase coupling is applied.

An analysis of the thermo-hydraulic performance, including the investigation of the interaction between particulate fouling and local flow structures, has been performed for sharp-edged spherical dimples in a staggered arrangement using Eulerian-Lagrangian LES with a corresponding mass loading of $\eta = 0.2\%$. Using the common definition of the Darcy friction factor f, the full pressure loss can be expressed as:

$$f = -\frac{(dp/dx)D_h}{\rho_f u_b^2/2}, \tag{15}$$

where (dp/dx) represents the pressure gradient in streamwise direction, D_h is the hydraulic diameter of the channel, ρ_f and u_b are the density and the bulk velocity of the fluid, respectively. The convective heat transfer is evaluated in terms of the local Nusselt number:

$$Nu = \frac{hL}{k} = \frac{q(2H)}{(T_w - T_f)k}, \tag{16}$$

with the convective heat transfer coefficient h, the characteristic length L, the heat flux q and the thermal conductivity k of the fluid. In order to make the numerical results comparable to empirical correlations, an area-averaged Nusselt number is calculated as follows:

$$\overline{Nu} = \frac{1}{A}\int_A Nu\,\mathrm{d}A\,, \tag{17}$$

where A is the heat transfer surface area. The friction coefficient f_0 and Nusselt number Nu_0 of the smooth channel are determined using the well-known correlations proposed by Petukhov and Gnielinski (Bejan & Kraus (2003)) for pipe flows:

$$f_0 = (0.790\ln(Re_D) - 1.64)^{-2}, \tag{18}$$

$$Nu_0 = \frac{(f_0/8)(Re_D - 1{,}000)\,Pr}{1 + 12.7\,(f_0/8)^{1/2}\left(Pr^{2/3} - 1\right)}. \tag{19}$$

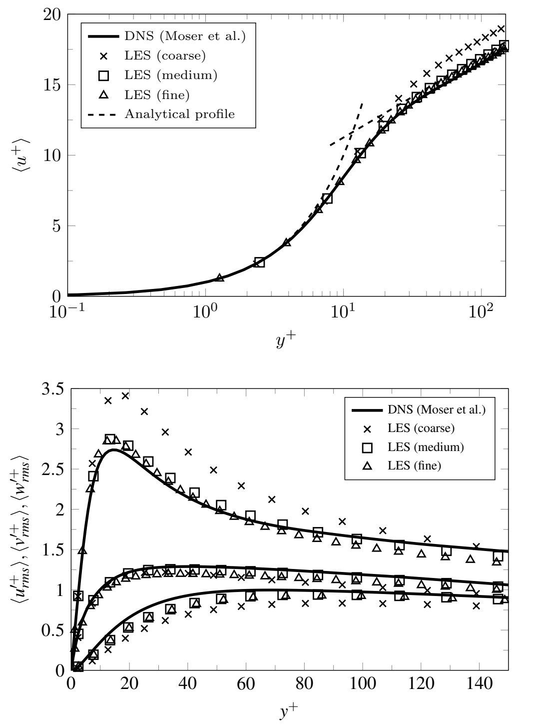

Figure 2. Mean streamwise fluid velocity profile $\langle u^+ \rangle$ and rms fluid velocity profiles $\langle u'^+_{rms} \rangle$, $\langle v'^+_{rms} \rangle$ and $\langle w'^+_{rms} \rangle$ in wall units.

These correlations are obtained for Reynolds number Re_D, based on the tube diameter, and are valid for a wide range of Prandtl numbers $0.5 \leq Pr \leq 2,000$ and $3,000 \leq Re_D < 5 \times 10^6$. Thus, Re_D has to be replaced by the appropriate Reynolds number based on the hydraulic diameter $D_h = 2H$ for a narrow, infinitely wide channel.

Table 5 presents the thermo-hydraulic performance analysis based on the obtained LES results and the empirical (smooth channel) correlations, Eq. (18 - 19), for the investigated clean dimple packages. Significant influence of the dimple depth becomes very clear, since the additional hydraulic loss f/f_0 due to the deep dimples ($t/D = 0.35$) is two times higher, compared to the shallow dimples ($t/D = 0.26$). Contrary to this observation, a comparable dependency between the heat transfer enhancement $\overline{Nu}/Nu_0$ and the dimple depth is not noticeable, whereby the heat transfer augmentation in case of the deep dimples is about 20% greater as for the shallow dimples, resulting in a slightly better thermo-hydraulic performance (approx. 5%) of the shallow dimples. Accordingly, the increase of the additional hydraulic loss caused by the larger dimple depth cannot be compensated by the heat transfer augmentation. This observations are generally in line with results published by Ligrani et al. (Ligrani *et al.* (2003); Ligrani (2013)) and Turnow et al. (Turnow *et al.* (2012)).

Table 1. Thermo-hydraulic performance analysis for clean dimples in a staggered arrangement at $Re_D = 42,000$.

t/D	f/f_0	$\overline{Nu}/Nu_0$	$\frac{(\overline{Nu}/Nu_0)}{(f/f_0)}$	$\frac{(\overline{Nu}/Nu_0)}{(f/f_0)^{1/3}}$
0.26	5.466	3.023	0.553	1.716
0.35	11.074	3.644	0.329	1.635

In Figure 3, the local flow structures caused by the different dimple packages are visualized by streamline patterns phase-averaged over a corresponding time interval of $t = 0.5\,$s. This illustration shows clearly the strong mixing and high complexity of the flow, which is more or less stochastic without distinctive coherent structures, as reported for the single spherical dimple (Kasper *et al.* (2017, 2018); Turnow *et al.* (2018)). The perturbations, coming from the upstream located dimples, destroy and break down the large, organized structures into small scale eddies (Turnow *et al.* (2012)). Especially for the shallow dimples at $t/D = 0.26$, the identification of coherent structures is very difficult. However, some typical flow structures can be recognized from the phase-averaged streamlines, for instance the reverse flow with a strong recirculation zone inside the dimples. A certain part of the incoming fluid attaches the downstream side and leaves the dimple directly at the trailing edge, while the main part of the arriving flow enters the dimple, rotates and is finally ejected over the dimple side edge into the main flow. Moreover, the flow structures produced by the deep dimples are more concentrated and causes higher flow velocities, primarily in the channel flow above the dimples. Figure 4 and 5 shows the time-averaged convective heat transfer in terms of the Nusselt number $\langle Nu \rangle$ (normalized by the Nusselt number Nu_0 for the smooth, narrow channel) as well as the wall shear stress $\langle \tau_w \rangle$ at the clean, dimpled bottom wall for both dimple package configurations. The highest heat transfer rates are observed, independently from the in-

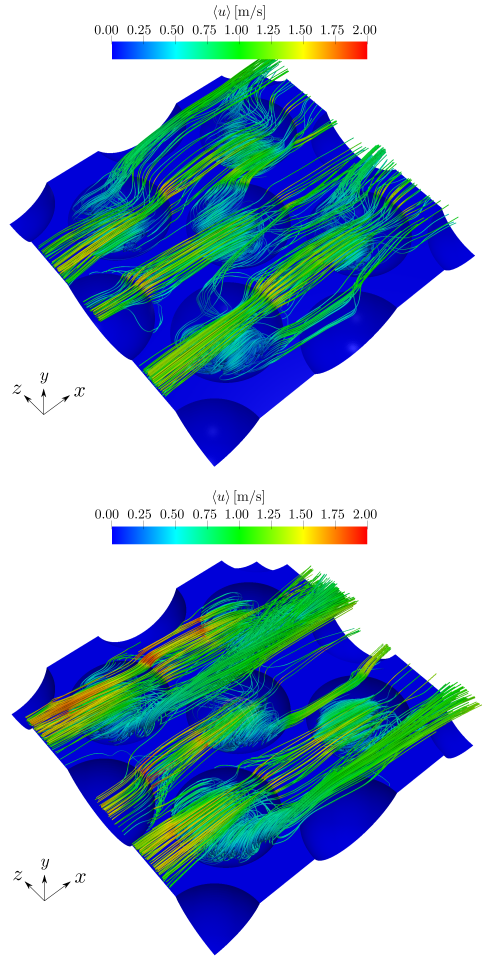

Figure 3. Phase-averaged streamline patterns for $t = 0.5\,$s inside a dimple package with different dimple depths at $Re_D = 42,000$: $t/D = 0.26$ (above) and $t/D = 0.35$ (below).

vestigated dimple depth, at the downstream side and trailing edge of the dimple, where cold flow attaches the surface and maximum flow velocities occur. For the deep dimples it can be up to eight times higher than for the smooth channel. Additionally, the stable recirculation zones within the dimples are responsible for a remarkable reduction of the heat transfer augmentation at the upstream side of the dimples. This region of low heat transfer rate is more pronounced for the shallow dimple package ($t/D = 0.26$), resulting in 20% lower overall heat transfer enhancement in comparison to the deep dimples.In contrast to previous experimental (Ligrani *et al.* (2003)) and numerical investigations (Turnow *et al.* (2012)= of dimpled surfaces, no optimal dimple depth-to-diameter ratio concerning a maximum thermo-hydraulic performance, could be determined. The reason for this observation is the relatively low channel height to dimple depth ratio of $H/D = 0.326$, since the vortex structures, generated by the dimples, are very large, in respect of the restricted channel height. This results in stronger perturbations, higher mixing and a significant acceleration of the mean fluid flow. Consequently, higher, time-averaged wall shear stresses $\langle \tau_w \rangle$ can be observed at the bottom wall between the dimples and at the trailing edges, which have a substantial influence on the fouling distributions, presented in Figure 6 for 120 s of physical real time and a foulant particle mass loading $\eta = 0.2\%$. Opposed to the single spheri-

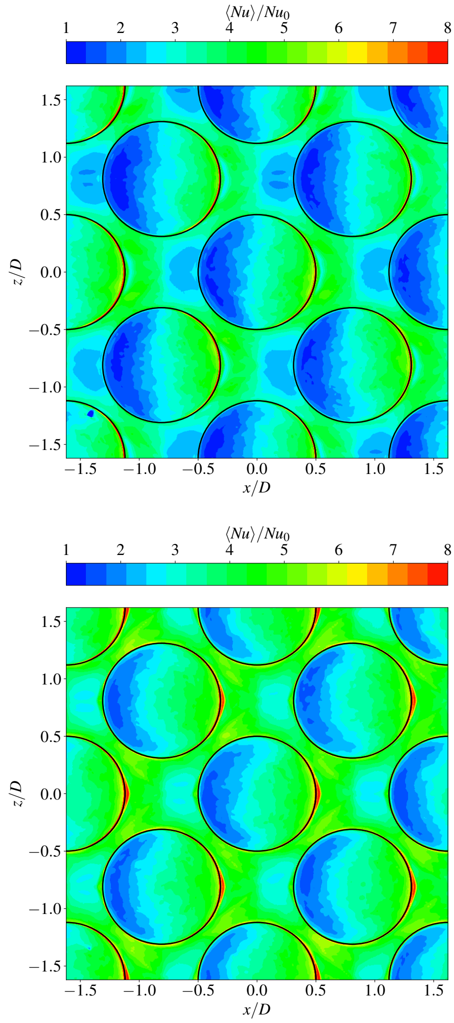

Figure 4. Time-averaged Nusselt number distribution $\langle Nu \rangle / Nu_0$ at the clean, dimpled bottom wall at $Re_D = 42,000$: $t/D = 0.26$ (above) and $t/D = 0.35$ (below).

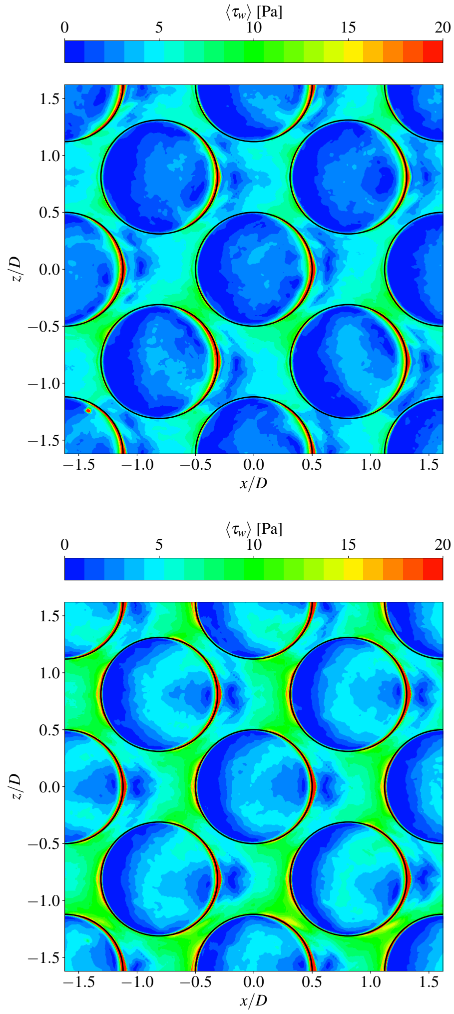

Figure 5. Time-averaged wall shear stress distribution $\langle \tau_w \rangle$ at the clean, dimpled bottom wall at $Re_D = 42,000$: $t/D = 0.26$ (above) and $t/D = 0.35$ (below).

cal dimple (Kasper *et al.* (2017, 2018)), the simulated fouling layers for both dimple package configurations are very disturbed and not evenly distributed. The main reason for this observation is the high turbulence intensity and mixing within the fluid flow, produced and enhanced by the dimples, which acts as turbulence generators. However, an identification of typical regions in the fouling layer is possible, for example the relatively high fouling layer thickness inside the recirculation zones within the dimples, caused by lower fluid velocities and wall shear stresses. The fouling layer thickness in this particular region is up to $x_f = 100\,\mu$m for the deep dimples and about $x_f = 80\,\mu$m for the shallow dimples. It is assumed, that a larger amount of the relatively heavy glass particles is not able to leave the deeper dimples, resulting in higher fouling rates. In contrast, the high wall shear stresses in the downstream side of the dimples mitigate particle depositions. Similarly, the wall shear stresses avoid the build up of evenly distributed fouling layers with large thicknesses on the remaining bottom wall, outside of the dimples. Solely for the shallow dimples, more particulate fouling occurs in the web region and in front of the dimples, amplified by lower fluid velocities and a stronger stagnation of the mean flow upstream of the dimples. This leads to a slightly higher overall amount of particulate fouling in case of the shallow dimples, which is contradictory to our previous observations for the single spherical dimple. However, this findings can be explained by the completely different flow features, generated by a single dimple compared to several dimples in a staggered arrangement. However, further investigations for larger times of simulation are necessary for reliable final conclusions. A noticeable influence of the particulate fouling on the hydraulic losses and heat transfer, after a physical real-time of 120 s, cannot be determined, due to the relatively thin fouling layer. Thus, the main objective for the future work is the development of an appropriate method in order to extend our results to larger fouling intervals.

CONCLUSION

Eulerian-Lagrangian LES of particulate fouling for different dimpled surfaces, namely the single spherical dimple and spherical dimples in a staggered arrangement, were carried out, including phase coupling and sub-models to consider the formation and removal of fouling deposits. The efficiency of the proposed numerical approach is enhanced by the introduction of an additional algorithm, which converts deposited particles from the Lagrangian frame into the Eulerian frame of reference. Thus, the number of active and tracked particles within the computational domain is kept

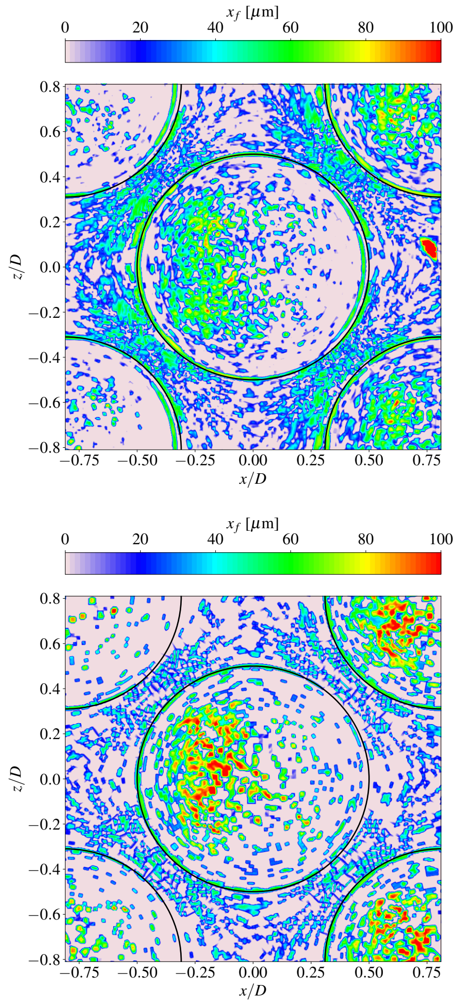

Figure 6. Distribution and thickness x_f of fouling layer after 120 s of physical real time for a foulant particle mass loading $\eta = 0.2\%$ and $Re_D = 42{,}000$: $t/D = 0.26$ (above) and $t/D = 0.35$ (below).

nearly constant. Due to the relatively low mass loading of $\eta = 0.2\%$ the inter-particle interactions could be neglected whereby the computational effort is strongly reduced.

Study of the dimple package with a staggered arrangement of dimples with $t/D = 0.35$ reveals generation of local vortex structures which are in a narrow channel ($H/D = 0.326$) much larger and stronger than those in the package with shallow dimples $t/D = 0.26$. These vortices promote stronger perturbations, a significant acceleration of the mean fluid flow at the wall and consequently higher wall shear stresses, avoiding the build up of fouling formations on the surface between the dimples. Thus, a slightly lower overall amount of particulate fouling can be observed for the deep dimple package, which is contradictory to our previous observations for the single spherical dimple (Kasper *et al.* (2017, 2018)). This opposite finding is explained by completely different flow features generated by a single dimple in comparison with a dimple package.

REFERENCES

Bejan, A. & Kraus, A. D. 2003 *Heat Transfer Handbook*. John Wiley & Sons.

Blöchl, R. & Müller-Steinhagen, H. M. 1990 Influence of particle size and particle/fluid combination on particulate fouling in heat exchangers. *Can. J. Chem. Eng.* **68** (4), 585–591.

Bohnet, M. 1987 Fouling of heat transfer surfaces. *Chem. Eng. Technol.* **10** (1), 113–125.

Combest, D. P., Ramachandran, P. A. & Dudukovic, M. P. 2011 On the gradient diffusion hypothesis and passive scalar transport in turbulent flows. *Ind. Eng. Chem. Res.* **50**, 8817–8823.

Crowe, C. T., Sharma, M. P. & Stock, D. E. 1977 The particle-source-ln cell (psi-cell) model for gas-droplet flows. *J. Fluids Eng.* **99** (2).

da Silva, C. B. & Pereira, J. C. F. 2007 Analysis of the gradient-diffusion hypothesis in large-eddy simulations based ontransport equations. *Phys. Fluids* **19**, 1–20.

Germano, M., Piomelli, U. & Cabot, W. H. 1991 A dynamic subgrid-scale eddy viscosity model. *Phys. Fluids* **3** (3), 1760–1765.

Kasper, R., Deponte, H., Michel, A., Turnow, J., Augustin, W., Scholl, S. & Kornev, N. 2018 Numerical investigation of the interaction between local flow structures and particulate fouling on structured heat transfer surfaces. *Int. J. Heat Fluid Flow* **71**, 68–79.

Kasper, R., Turnow, J. & Kornev, N. 2017 Numerical modeling and simulation of particulate fouling of structured heat transfer surfaces using a multiphase Euler-Lagrange approach. *Int. J. Heat Mass Transfer* **115**, 932–945.

Kern, D. Q. & Seaton, R. A. 1959 A theoretical analysis of thermal surface fouling. *Brit. Chem. Eng.* **4** (5), 258–262.

Kim, W. & Menon, S. 1995 A new dynamic one-equation subgrid-scale model for large eddy simulation. In *AIAA, Aerospace Sciences Meeting and Exhibit, 33 rd, Reno, NV*.

Ligrani, P. M. 2013 Heat transfer augmentation technologies for internal cooling of turbine components of gas turbine engines. *Int. J. Rotating Mach.* **2013**, 1–32.

Ligrani, P. M., Blaskovich, T. & Oliveira, M. M. 2003 Comparison of heat transfer augmentation techniques. *AIAA Journal* **41** (3), 337–362.

Müller-Steinhagen, H. M. 2010 *VDI Heat Atlas - Fouling of Heat Exchanger Surfaces*. Springer-Verlag Berlin Heidelberg.

Putnam, A. 1961 Integrable form of droplet drag coefficient. *ARS Journal* **31**, 1467–1470.

Sommerfeld, M. 2010 *VDI Heat Atlas - Particle Motion in Fluids*. Springer-Verlag Berlin Heidelberg.

Taborek, J., Hewitt, G. F. & Afgan, N. 1984 *Heat exchangers: theory and practice*. Editors Hemisphere Publishing Corp.

Tsuji, Y., Tanaka, T. & Ishida, T. 1992 Lagrangian numerical simulation of plug flow of cohesionless particles in a horizontal pipe. *Powder Technol.* **71** (3), 239–250.

Turnow, J., Kasper, R. & Kornev, N. 2018 Flow structures and heat transfer over a single dimple using hybrid urans-les methods. *Comput. Fluids* **172**, 720–727.

Turnow, J., Kornev, N., Zhdanov, V. & Hassel, E. 2012 Flow structures and heat transfer on dimples in a staggered arrangement. *Int. J. Heat Fluid Flow* **35**, 168–175.

Yoshizawa, A. 1982 A statistically-derived subgrid model for the large-eddy simulation of turbulence. *Phys, Fluids* **25** (9), 1532–1538.

Yoshizawa, A. & Horiuti, K. 1985 A statistically-derived subgrid-scale kinetic energy model for the large-eddy simulation of turbulent flows. *J. Phys. Soc. Jpn.* **54** (8), 2834–2839.